Effect of power distribution on the weld quality during hybrid laser welding of an Al-Mg alloy

Original Citation:
Effect of power distribution on the weld quality during hybrid laser welding of an Al-Mg alloy / Leo, P; Renna, G.; Casalino, Giuseppe; Olabi, A. G.. - In: OPTICS AND LASER TECHNOLOGY. - ISSN 0030-3992. - 73:(2015), pp. 118-126. [10.1016/j.optlastec.2015.04.021]

Published version
DOI:10.1016/j.optlastec.2015.04.021

Publisher:

Effect of power distribution on the weld quality during hybrid laser welding of an Al-Mg alloy

P. Leo[1], G. Renna[1], G. Casalino[2*], A. G. Olabi[3]

[1] Innovation Eng. Dept. University of Salento, Via per Arnesano s,n, 73100 Lecce, Italy

*Corresponding author g.casalino@poliba.it

[2] DMMM, Politecnico di Bari, Viale Japigia, 182, Bari, Italy.

[3]Institute of Engineering and Energy Technologies, University of the West of Scotland, Paislae, PA1 2BE, Scotland

Abstract

This paper treats of the analysis of the effect of arc and laser powers on the quality of the arc assisted fiber laser welding of an Al-Mg alloy in butt configuration. Grain size, weld geometry defects, porosity, and magnesium loss were measured. Magnesium content of the fused zone decreased as the laser power increased while the porosity increased with laser power. Microhardness profiles and tensile properties were explained on the base of the joint microstructure and defects and related to the power distribution. The porosity level and Mg content in the fused zone affected both tensile strength and ductility. The power distribution that stabilized the welding process and minimize the weld porosity was defined.

Key-words: fiber laser, hybrid welding, Al-Mg alloy, weld quality, power distribution.

List of symbols and acronyms

ACZ	arc crown zone	MIG	metal inert gas
BM	base material	Nd:YAG	neodymium:yttrium aluminium garnet
CZ	crown zone	OM	optical microscope
DCZ	depth of crown zone (mm)	P_L	laser power (W)
DLZ	depth of laser zone (mm)	P_{MIG}	arc power (W)
DU	depth of underfill (mm)	P_{TOT}	total power of the heat sources (W)
E	elongation (%)	R	ratio between laser and MIG power
EDS	energy dispersive spectrometry	SEM	scanning electron microscope
FGZ	fine grain zone	TS	tensile strength (MPa)
FZ	fused zone	WCZ	width of crown zone (mm)
GMA	gas metal arc	WFR	wire feed rate (mm/min)
HAZ	heat affected zone	WLZ	width of laser zone (mm)
HLAW	hybrid laser-arc welding		
LZ	laser zone		

1. Introduction

For many years, both arc and laser welding have been the dominant joining methods of metals [1, 2]. Conventional electric arc welding processes show important advantages due to their availability, energy efficiency, simple technology and low costs of operation but meanwhile have some disadvantages such as process instability and slowness, a wide heat-affected zone (HAZ) and weldment distortion. In the same way, laser welding has some limitations and problems such as higher power consumption, high cost of equipment, poor bridgeability, strict requirements concerning the laser beam adjustment and sample alignment [3, 4]. Besides, laser welding generates welding bead with high pores/voids and is generally more difficult to apply to aluminum alloys, such as 5000 magnesium series. Those aluminum alloys, whose major alloying element is Mg, are desired for their excellent corrosion resistance, substantial strength and weldability [5, 6, 7]. Laser beam welding of Al alloy is particularly critical owing to high thermal and electrical conductivity, large thermal expansion, lower viscosity and high reflectivity of the metal [8]. During laser welding, the low melting point of the alloying elements such as magnesium or zinc easily makes them to vaporize [9]. Elements vaporize, escape through the keyhole, and pull molten material along with them, leaving weld voids and spatter in their wake. A homogeneous liquid forms prior to solidification when intermetallic compounds can form [10]. The formation of porosity, solidification cracking, and modification of the mechanical properties is the result of the element loss [11, 12]. Recently the laser-arc hybrid welding process has proved to be successfully to overcome problems commonly encountered during either laser or arc welding. Hybrid welding couples processes arc and laser welding in a single process. Hybrid welding overcomes the disadvantages in laser welding and in arc welding while keep advantages of both processes. Lower energy input is obtainable compared to arc welding therefore the welded structure has less thermal distortions and residual stresses. Moreover the hybrid laser arc welding (HLAW) reduces the need for edge preparation, it generates narrower heat-affected zone lower porosity while increasing welding speed and productivity [13, 14].

The laser-to-arc powers ratio also can play a significant but not enough clarified role in the hybrid welding process. That ratio determines which one between the laser and the arc is the dominant welding source and which one has the greater influence on the change in penetration depth and the width of the weld pool. El Rayes et al. reported that increasing the ratio of arc to laser power, for constant CO_2 laser power levels of 8 and 4 kW, causes the narrow lower portion of the hybrid weld cross-section to increase in length. However, it appears to be a minimal effect on the total depth of the weld pool [15]. The change of the hybrid weld geometry according to laser/arc power ratio also alters mechanical properties of the joint [16]. Chen et al. [17] investigated the transition between conduction mode and keyhole mode with different energy ratios between laser and arc of CO_2 laser TIG paraxial hybrid welding. Moreover, a series of CO_2 laser–metal inert gas arc hybrid welding experiment investigated the effects of laser/arc energy ratio and groove parameters on the shape and microstructure of weld. In particular, M. Gao et al showed that increasing arc current and groove cross-section area can reduce the size of laser and arc zone by enhancing the uniform of energy distribution in the molten pool [18]. Detail studies on the interaction between laser radiation and electric arc used in hybrid heat source are available. During the pulsed laser-arc welding process the extension of arc plasma column into laser keyhole gives the pressure to the inner keyhole wall, which hinders the keyhole-collapse. Moreover, the surface tension of the liquid metal around the keyhole outlet increases due to the extension of arc column into the keyhole, which also prevents the keyhole outlet from collapsing [19]. As a synergetic effect of laser and arc the stability, the escaping ability of the gas bubbles in the weld pool increases [20, 21]. Katayama et al. has reported that an increase in arc current helped to prevent significantly the internal porosity formation due to a more favorable direction of the melt flow [22].

The fiber laser beam has a wavelength of one-tenth of that emitted by a conventional CO_2 laser and it ensures high-speed results even when processing reflective materials, such as aluminum, and combination of dissimilar light metals [23, 24]. Thus far, this new kind of laser has showed higher efficiency in comparison to conventional solid-state (CO_2 and Nd:YAG) laser. During fiber laser-MIG hybrid welding, the pure argon shielding gas promotes the ionization and stabilization of the arc. Therefore, the fiber laser hybrid welding has demonstrated to warrant a more stable process. A common result in the performed investigation indicated that the strength loss of the joint strongly depends on magnesium loss, the decrease of the precipitates and the grain size growth. The porosity is also the main reason for the decrease of both tensile and fatigue strength [25, 26].

In this study, 3 mm thick AA5754-H111 aluminum alloy sheets were joined in the butt configuration using a fiber laser and a metal inert gas (MIG) arc welding process. The quality characteristics of weld bead geometry, macro and microstructure, micro-hardness and defect formation of the joints were analyzed and discussed with respect to the power distribution, which is an alternative to the classic process parameters approach [27]. The scopes of this article is to give a detailed characterization of the weld metallurgical and mechanical properties and to relate phenomena like segregation and porosity to the arc and fiber laser power. The process condition to obtain good mechanical properties and low-porosity weld were identified. Eventually, recommendation for a stable welding process was given.

2. Laser and experimental set-up

The base material used in this study was an AA5754-H111 plates whose thickness was 3 mm. AA 5754-H111 alloy is one of the 5XXX series non-age hardenable aluminum-magnesium (Al-Mg) alloy whose magnesium is the major alloying element. The suffixes H1 indicate the strain-hardened condition and the number following this designation indicates the degree of the strain hardening. Prior to welding, the Al alloy was in annealed and recrystallized condition. The wire was the commercial ER5356 one. Chemical compositions of the base metal and the filler wire are listed in Table 1.

Table 1 Chemical compositions of BM (Al 5754-H111) and filler wire (ER5356), (wt%).

Composition	Si	Fe	Cu	Mn	Mg	Cr	Zn	Ti	Al
5754-H111	0.4	0.4	0.1	0.5	2.6-3.6	0.3	0.2	<0.15	balance
ER5356	0.25	0.4	0.05	0.1-0.2	4.5-5.5	0.1-0.2	0.1	0.15	balance

The welding experiments of AA5754-H111 were carried out by an Ytterbium Laser System (IPG YLS-4000; maximum output power is 4 KW) in combination with MIG welding machine (GENESIS 503 PSR). The welding layout is depicted in figure 1. The experiment configuration was laser leading, which means that the laser beam is the primary heat source while the arc is the assisting heat source. Argon was the shielding gas. Detail information on the hybrid laser/MIG welding equipment are in table 2.

Table 2 Experimental parameters and levels at-a-glance.

Laser (IPG YLS-4000)	
Beam wavelength (nm)	1070.6
Focus spot diameter (mm)	0.4
Focal distance of lens (mm)	250
Diameter fiber (μm)	200
Beam Parameter Product (BPP) (mm*mrad)	6.3
Focal position	weld surface
Welding speed (m/min)	3.5

Shielding gas	Argon 25 l/min
MIG generator (GENESIS 503 PSR)	
Torch position	wire tip 2.5 mm behind laser
Torch inclination angle	40° from weld surface
Filler wire	Er5356

The joint was in butt configuration. The laser power (P_L), wire feed rate (WFR), and arc power (P_{MIG}) varied accordingly with the following experimental plan, The P_L was constant while the P_{MIG} varied on three levels, the welding speed was 3,5 m*min^{-1}The arc power (P_{MIG}) is the product of the arc current intensity (A) and the arc voltage (V). R indicates the ratio between the P_L and the P_{MIG}. Table 3 shows the parameters levels for each welding condition.

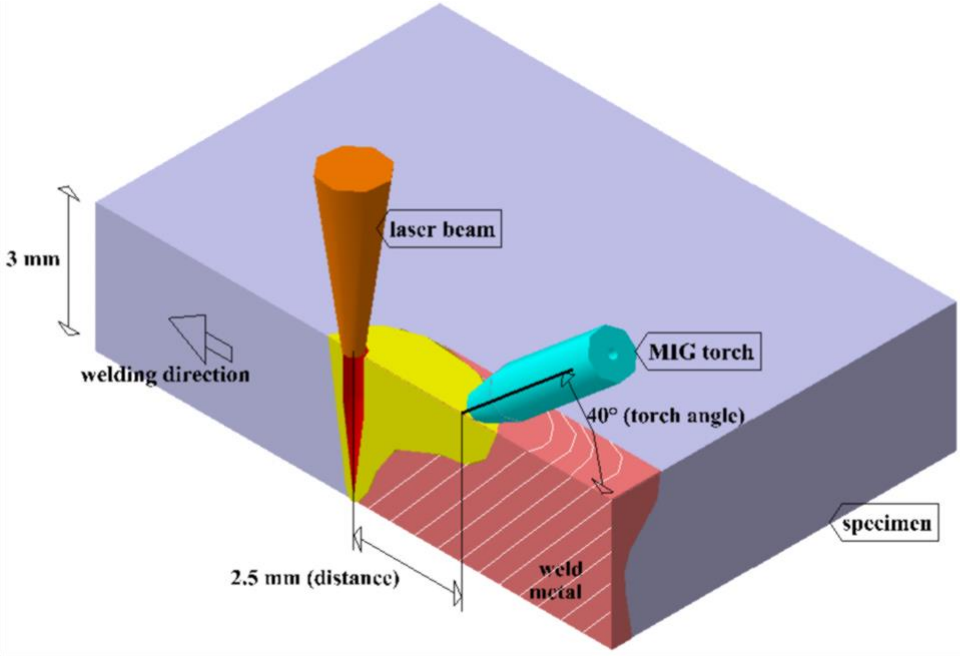

Fig. 1. Normal hybrid welding layout.

Weld transverse cross sections were cold mounted. Then they were grinded and mechanically polished using a variable speed. After that, the specimens were etched using Keller reagent (1 ml HF, 1.5 ml HCl, 2.5 ml HNO_3, and 95 ml H_2O). The microstructures of the fusion zone, porosity and bead dimension for every welding condition were examined using the optical microscope (OM) Nikon Epiphot 200 and a computer-assisted image analysis (NIS Elements AR).

Subsequently, the macro-section of weld bead were ground according to the standard procedures afterwards each surface were electro polished by 20% $HClO_4$ and 80% C_2H_6O at 0°C with 15V and for 60s and finally were anodized by Barker's electrolyte in an electrolytic cell at room temperature with 20V for 80s. The etched samples were examined in OM under polarized light in order to determine the size and shape of the grain. A high-resolution macro-image of the transverse weld cross-section was reconstructed by tiling contiguous micrographs.

Table 3 Welding parameters (where $P_{TOT} = P_L + P_{MIG}$)

	MIG voltage (V)	**MIG current (A)**	**WFR (mm/min)**	**P_L (W)**	**P_{MIG} (W)**	**P_{TOT} (W)**	**R**
1	24.5	114	10.4	2500	2793	5293	0.895
2	26.5	128	11.4	2500	3392	5892	0.737
3	28	140	12.2	2500	3920	6420	0.638
4	24.5	114	10.4	3000	2793	5793	1.074
5	26.5	128	11.4	3000	3392	6392	0.884
6	28	140	12.2	3000	3920	6920	0.765
7	24.5	114	10.4	3500	2793	6293	1.253
8	26.5	128	11.4	3500	3392	6892	1.032
9	28	140	12.2	3500	3920	7420	0.893

The pores area was evaluated using NIS software for imaging analysis. Porosity percentage (pores area divided by the area of the fused zone) was determined for each joint.

The weld microstructure was analysed by scanning electron microscopy (SEM) Zeiss EVO after polishing and without any chemical etchant. The magnesium content in solid solution in the fusion zone was measured at mid thickness along the centerline of seam cross section by energy dispersive spectrometry (EDS) technique using a Brucker electron microprobe.

Vickers micro-hardness (0,5Kg/15s) was measured along the joint cross section at 1 mm from the top and bottom surfaces. Rectangular sample for tensile testing were cut from the weldment perpendicularly to the weld fusion line. Tensile strength test for the base material and hybrid joint was performed at room temperature on an INSTRON tensile machine, model 4485.

3 Microstructural Characterization of as received AA5754-H111

Either coarse intermetallic compounds/constituent particles (0.5-10 micron) and smaller submicron particles or dispersoids (typically 0.05-0.5 micron) characterized the microstructure of the strain-hardened AA5754-H111. The constituent particles usually contained iron such as $(Fe,Mn)Al_6$ and/or $(Fe,Mn)_3SiAl_{12}$ (white color in SEM micrograph Fig. 2a). The other detected phase was rich in magnesium and silicon Mg/Si (dark particles in Fig. 2a).

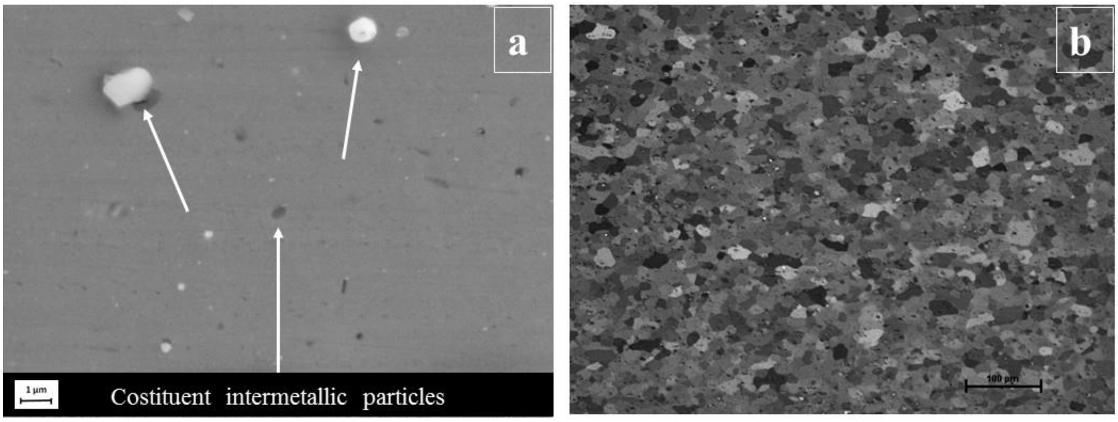

Fig. 2. Microstructure of parent alloy: a) BSE image containing iron particles (white colour) and magnesium-silicon rich particles (gray colour); b) optical image of the recrystallized grain structure after anodized with Barker’s reagent and under polarized light.

The iron rich intermetallic phases exhibited a good contrast with the surrounding alloy matrix in backscattered imaging mode. The smaller particles or dispersoids in Al-Mg alloys contained one of transition metals such as $Mg_{2/5}Al_{3/8}$, $Cr_2Mg_3Al_8$, $MnAl_6$ [28, 29]. The microstructure of the rolled plate was fully recrystallized and the average grains size was equal to 20 ± 5 μm (Fig. 2b). BM exhibited an average micro-hardness equal to 60 ± 0.8 HV. At room temperature, the tensile strength was 240 MPa and the elongation 16%.

4. Results and discussion

For welds numbered from 1 to 3, the severe porosity in the fusion zone produced unacceptable defects. The flow of liquid metal conveyed and pushed the gas bubbles towards the solidification front. There the bubbles gathered up and form an irregular porosity. Consequently, the keyhole was unstable and collapsed [9]. Thus, the following results and discussion concern with sample from 4 to 9.

4.1 Weld appearance and microstructure

In the cross sections of the joints, the fused zone (FZ) was characterized by wine-cup shape consisting of two zones (shown in Fig. 3) usually named laser zone (LZ) because its keyhole-like shape [14, 30] and arc crown zone (ACZ) or crown zone (CZ) (Fig. 3a).

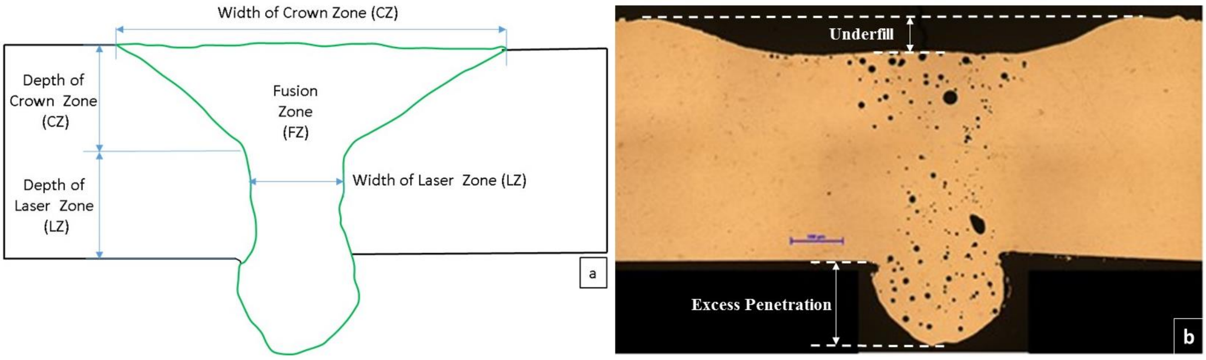

Fig. 3. a) cross section draft of the weld with the geometrical features of the fused zone, b) example of defects: porosity, excessive penetration (root drop-out) and under filling.

Fig. 4 shows polarized light optical micrographs. The CZ and LZ is easily identified, as well as the penetration excess.

Equiaxed grains were dominant in the weld centerline while close to the FZ/BM interface directional columnar solidification structure was observed from the fusion boundary down to the certain depth of FZ (Fig. 4, 5).

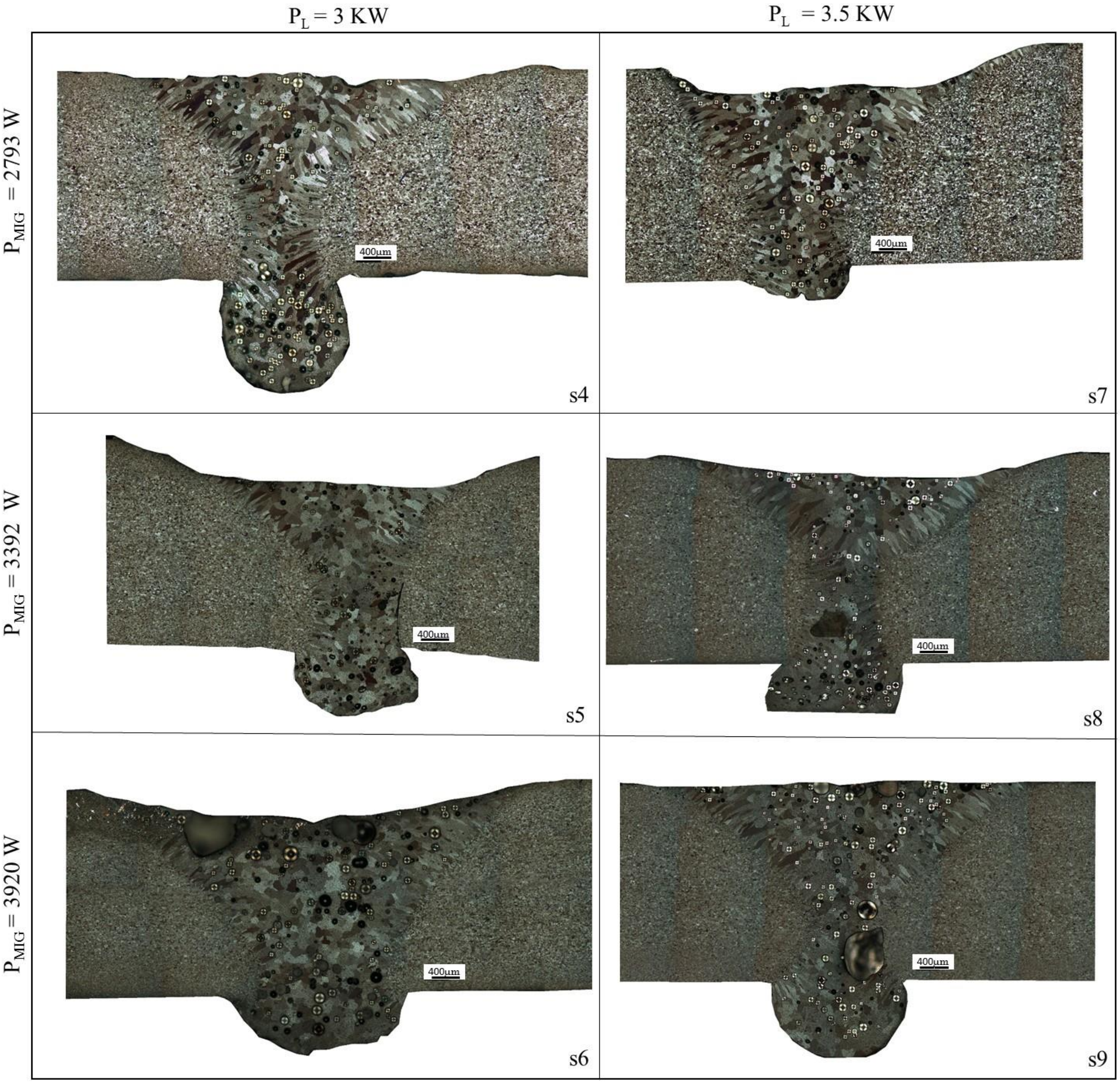

Fig. 4. Micrographs of butt weld beads cross-section of alloy 5754-H111 joints, as a function of the laser power and the arc MIG power.

After Keller etching, high magnification analysis of CZ and LZ microstructure was conducted at 1 mm from the top and bottom surface of joints along the weld axes and the FZ/BM interface.

At high magnification, the FZ microstructure (Fig. 5) presented equiaxed dendrites at the centerline and columnar dendrites close to the interface. Moreover, a zone characterized by fine equiaxed grains occurred at the FZ/BM interface (Fig. 5c). The thickness of the fine grain zone (FGZ) and its grain size did not change appreciably with the power distribution. The FGZ average thickness and grain size values were 65.5±14 µm and 16±5 µm, respectively. Weld microstructure is due to constitutional undercooling in the melt. When little undercooling occurred [31] (as at the interface between FZ and BM) epitaxial growth develops from many nuclei with the same lattice structure of the BM grains (Fig. 5). As undercooling increased, the formation of stable protrusions or dendrites occur into the melt zone leading to the formation of columnar grains (Fig. 4). Moving towards the weld centerline both the shallow thermal gradient and the increased fluid flow lead to the transition from columnar to equiaxial growth (Fig.4, 5, 6c).

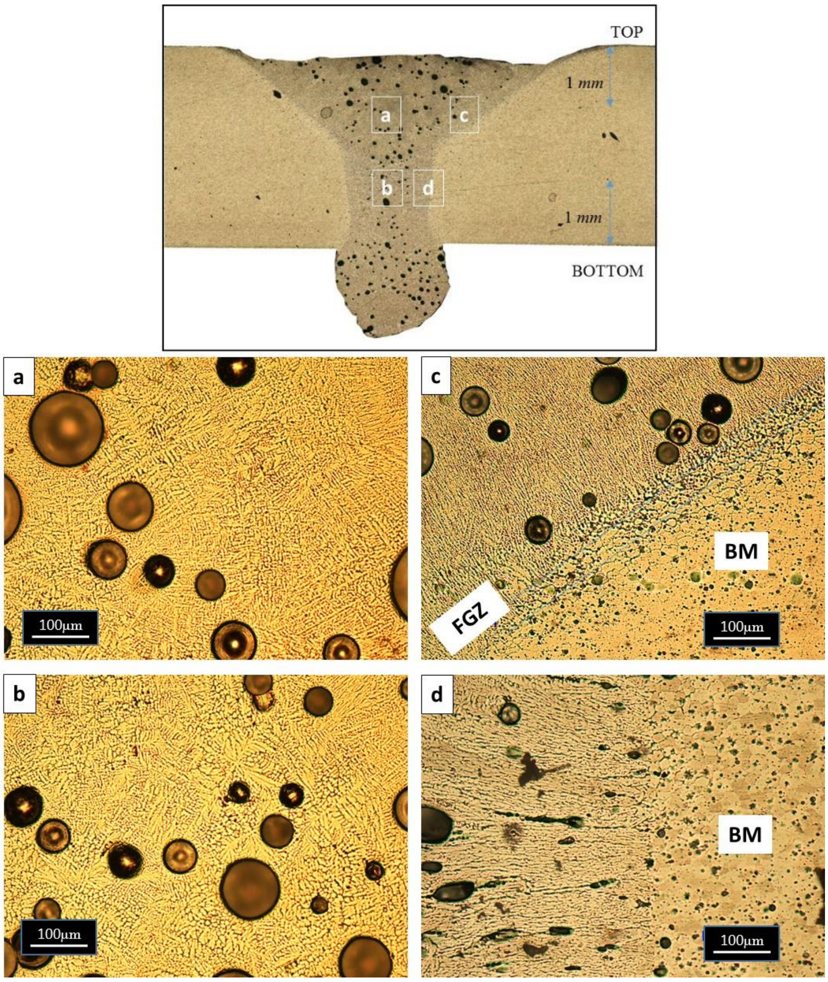

Fig. 5. Microstructure of the fused zone (FZ) and fine grain zone (FGZ) before the base metal (BM). Points were picked up at the point indicated in the macrography: crown zone (a and c) and laser zone (b and d).

Particularly a narrower area of equiaxial grain is observable in the LZ respect to the CZ (except for the 6 and 7 samples) (Fig. 4) due to the slightly variable thermal gradient, less sensitive to MIG process. So, the columnar grain stabilize and grow approaching to the centerline (Fig. 4) [32].

Solidification cracks (Fig. 5d) occurred mostly in the LZ along the columnar grain boundaries, which originated from the fusion zone edge (Fig 5d) where the molten pool would solidify faster respect to the fusion edge of the crown zone.

Solute segregation and second-phase affected the FZ microstructure along the centerline of the cross section (Fig. 6a). Inter-dendritic Chinese script phases containing iron (white in Fig. 6b) and non-equilibrium eutectic Mg/Si (black in fig.6b) were visible the FZ [33, 34]. Segregation was due to non-equilibrium solidification. Particularly, second-phase segregation is mostly evident along welding axes (Fig. 6a) due to larger undercooling and decreased close to the interface [35, 36, 37, 38].

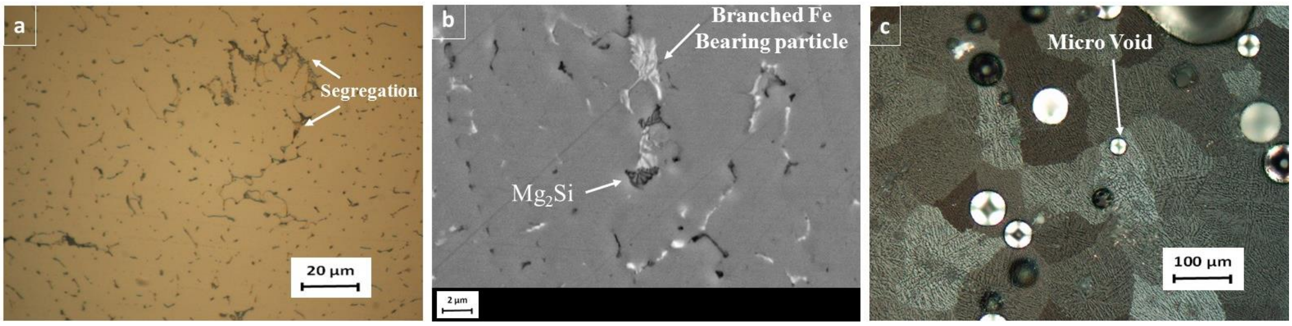

Fig. 6. a) OM image at the center of the cross section of the FZ showing centerline segregation b) high magnification BSE image of centerline segregation in FZ and the white arrow points to both Mg_2Si eutectic phase and iron-bearing intermetallic phase with branched/Chinese script morphology, c) polarized light optical micrograph of coarse equiaxed grains structure with pores in the FZ.

The grain size of the heat affected zone presented a strong variation inside the analyzed areas and its variation was higher in the grain size of the sample processed at lower laser power (3 KW). As the laser power increased (see samples 7, 8, and 9) the grain size became ~~more~~ uniform. Nevertheless, the joint average grain size was much higher than that of BM (Fig. 6c and Fig. 2b) which was equal to 20 µm. Figure 7 shows the relationship between power ratio and the grain average size. For R=0.89 (9) the MIG power contributed with 52.8% of the total welding power and became ~~more~~ dominant as R decreased. Conversely, the laser power contributed with 55.6% per cent of the total welding power and became less important as R decreased. When the power ratio was larger than 1, the average grain sizes was lower and almost constant respect to the one with R<1. In fact, the higher P_L percentage leads to a faster cooling that reduced the grain size [39]. Moreover, for R>1 the reduced influence of P_{MIG} led to a uniform thermal gradient and to a grain size that had a lower standard deviation respect to the samples processed at R<1 [31, 32, 39]. When P_{MIG} decreased, the smaller average grain size was obtained when R was closest to 1. So, in both cases (R<1 and R>1), the lower average grain size was obtained for R values closest to 1. Moreover, the samples processed at P_L equal to 3 KW exhibited an average grain size that increased with P_{MIG} (compare 4, 5, 6) while for samples processed at 3.5 KW (7, 8, 9) the average grain size was less dependent on P_{MIG}.

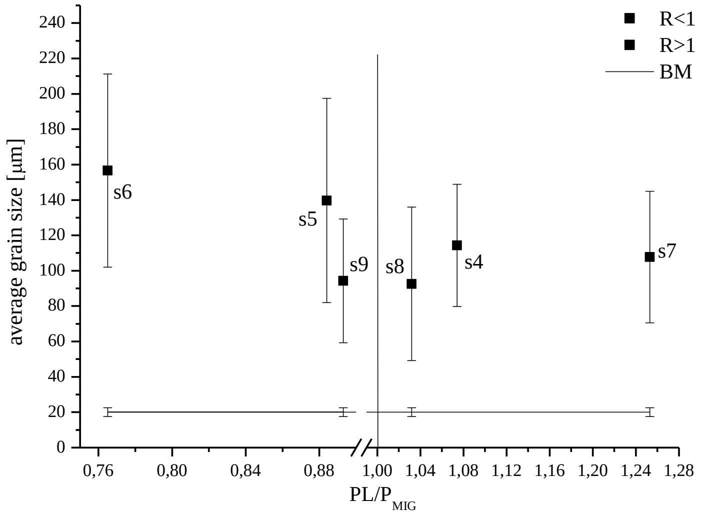

Fig. 7. Relationship between average grain size across the cross-section of the FZ and power ratio (P_L/P_{MIG}).

The Mg contents in the solid solution (weight %) of each joint was obtained by EDS analysis along the cross section welding axis at the mid thickness. The same area was analyzed for each sample. Figure 8 shows the results.

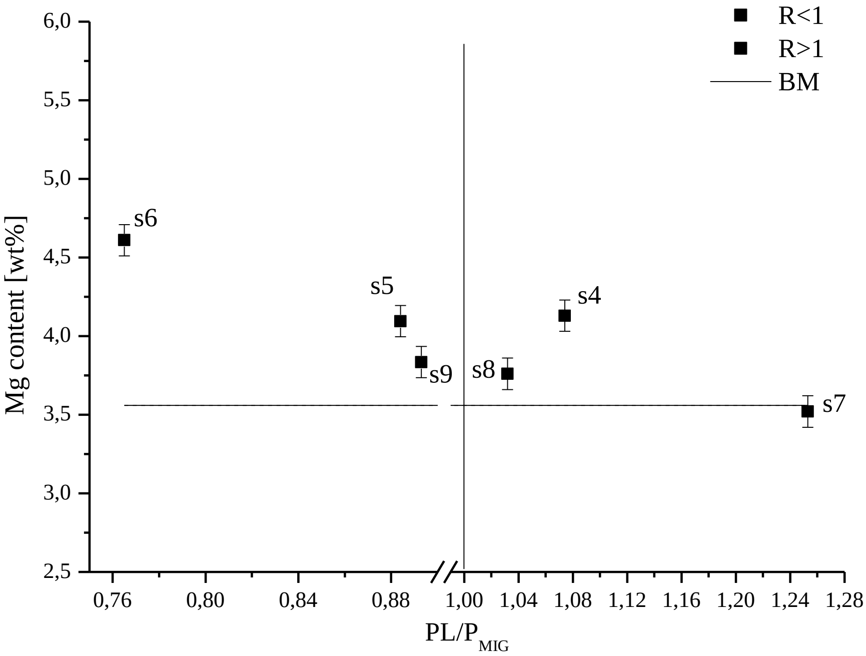

Fig. 8. Influence of R (P_L/P_{MIG}) on the magnesium concentration in the fused zone.

There difference in Mg content between the different welds was not important. Sample 6 had the highest Mg content. It is noteworthy that the average Mg content in all the samples, apart from 7, was always higher than that of BM (Table.1). The samples processed at highest laser power (7, 8, 9) exhibited a lower Mg content respect to those processed at lower P_L. This difference could be due to the Mg vaporization promoted by highest laser power [40]. Mg content was lower when the laser power increased (6-9, 5-8, 4-7) for the same P_{MIG}. Mg content increased with P_{MIG} for the same P_L (Fig. 8). When supplying more filling wire, P_{MIG} increased and so did the Mg content. The joint processed at similar power ratio-values (5, 9 and 8, 4) had similar average Mg content. Grain size and Mg content exhibited similar trend with respect to R.

4.2 Weld Geometry

The width and depth of CZ (respectively WCZ and DCZ), of LZ (respectively WLZ and DLZ) and underfill depth (DU) were measured. In Fig. 9, those data are showed as a function of the R ratio.

As R ratio approaches to the unit, WCZ, DCZ, WLZ and DU assumed closer values. As R moved away from unit DCZ, WLZ and DU slightly increased meanwhile WCZ become lowest at the highest R (7) and vice versa (6). WCZ increasing with decreasing power of ratio from 1.28 (7) to 0.7 (6) was due to the MIG power contribute [41]. For high P_{MIG}, a higher portion of BM in the outlet keyhole fused under the action of the electric arc, which increased WCZ. At fixed MIG power, the WCZ was lower for the samples processed at higher laser power because of the stabilization effect induced on MIG arc by higher P_L [40,42].

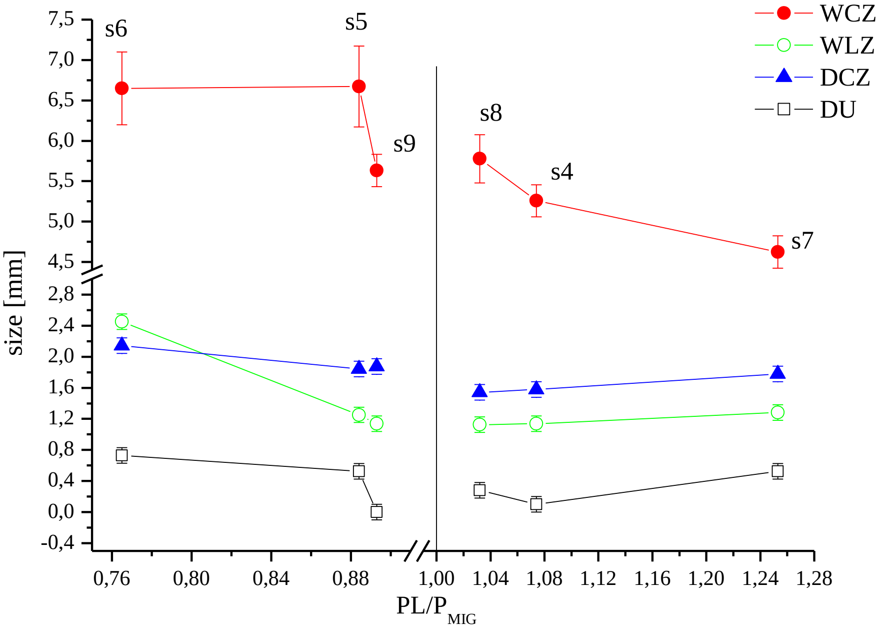

Fig. 9. Effects of power ratio R (P_L/P_{MIG}) on the weld shape. The width crown zone, width laser zone, depth crown zone and the underfill depth of weld cross-section corresponding to each power ratio are illustrated.

The highest WLZ was observed in samples 6 and 7, which were characterized by the deepen DU. Considering the samples processed at the lowest P_L (4, 5, 6), DU increased with P_{MIG}. As P_{MIG} increased, the arc force possibly started to work at the outlet of the keyhole instead of acting at the inner of the keyhole, which rose DU [43]. On the contrary, at P_L equal to 3.5 KW (7, 8, 9), DU increased with decreasing P_{MIG} being maximum in sample 7. As discussed above, the MIG arc was more stable at the highest P_L when Mg vaporization is favored (Fig. 8). Mg vaporization, leading to higher vapor pressure, pushed the melt towards the joint bottom causing expulsion of the molten metal and a metal vacancy at the joint top. For sample 7, the wire was unable to fill the lack due to the low wire feeding rate [9], so the highest DU was observed. As P_{MIG} increased, the depression due to the high vapor pressure was filled by the feeding wire and so DU decreased (Fig. 8). Therefore, the highest and lowest R ratio produced defects that were due to Mg vaporization/inadequate filling and to arc pressures that work at the outlet of keyhole.

The joints with close R had also similar geometry. The joints characterized by R close to 1was symmetric respect to the centerline (Fig. 4) with CZ and LZ profiles well defined and a better process stability respect to the samples processed at the other R values.

4.3 Porosity

Microporosity was analysed along the weld. The fraction area of pore was calculated in the CZ and LZ and it is reported in Table 4 and Fig.10. The pore distribution was random within the weld and the diameters varied between 20-150 μm. The micropores might have formed during the welding of the aluminum alloys due to the high solubility of the hydrogen in the liquid aluminum and vaporization of the alloying elements like magnesium [44, 45]. Fig. 10 shows the total porosity in the fusion zone as function of R ratio. Porosity area fraction increased with laser power (7, 8, 9), which favored Mg vaporization. The absolute value of porosity assumed the highest values at the extreme R ratio. It is interesting to observe that in the range of analyzed R there was no strong variation in the porosity. Moreover, the trend of porosity versus R was opposite to that of Mg versus R, except for sample 6, for which the porosity did not depend on the Mg content because of the arc instability.

The negative effect of porosity was mainly the concentration of stress on pores and reduction of useful area for mechanical resistance. The ductility and tensile strength decreased.

Table 4 Porosity area fraction in CZ, LZ and FZ (FZ=area CZ + area LZ).

sample	CZ (%)	LZ (%)	FZ (%)
1	28.4	50.4	33.6
2	14.4	78.4	29.8
3	8	28.4	13.6
4	4.2	5.2	4.5
5	3.8	5.4	4.2
6	6.2	4	4.9
7	10.2	6.6	8.5
8	7	5.2	6.1
9	6.1	6.4	6.2

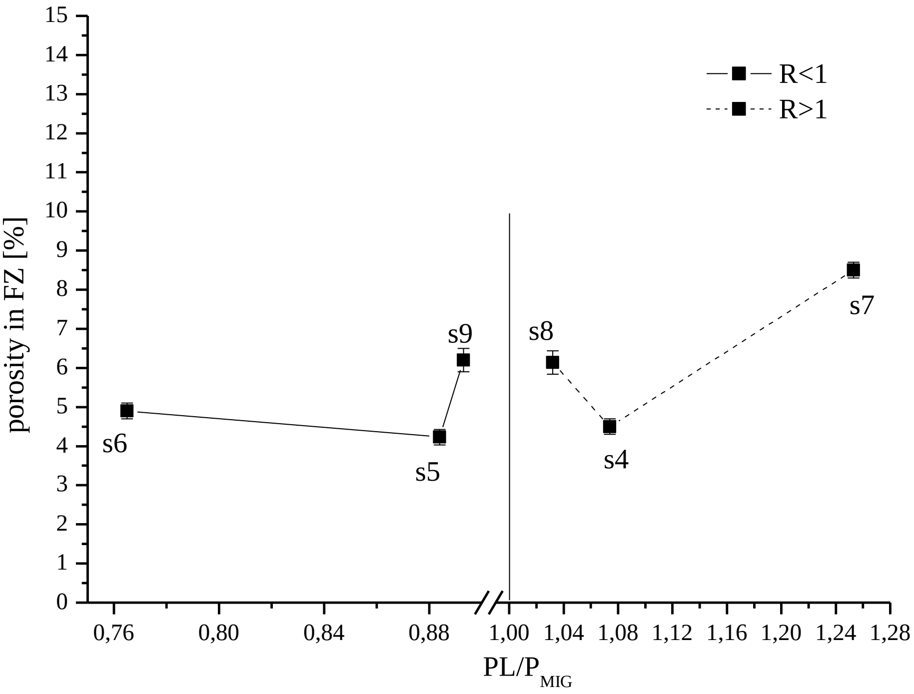

Fig. 10. Relationship between FZ porosity [%] and power ratio.

4.4 Mechanical properties

The main mechanisms of hardening for the Al-Mg alloys are both Mg solid solution and grain boundary strengthening [26, 46, 47]. Fig. 11 shows the micro-hardness profiles in the CZ and LZ zone of samples 5 and 8 at 1 mm from the bottom/top of joints. The micro hardness profiles were almost symmetric respect to the weld centerline, where the hardness reached the lowest values. All the hardness values in FZ were higher or equal to those of BM (except at place very close to the centerline), which can be explained with the higher Mg content of weld induced by filling wire overcoming the softening induced by the coarse grain size. At the center line a high segregation level was observed (Fig. 6a, b) due to the large undercooling [21, 23, 24]. As segregation reduced the mechanical properties, the lowest hardness values along welding axis probably depended on the high segregation level. Then, as segregation decreased moving from FZ centerline [31], the hardness values increased reaching a value much higher respect to BM in the FGZ, which was the hardest and minimum average grain size zone of the joint. In the HAZ, the hardness was higher than that of BM. Comparing CZ and LZ hardness values, the absolute minimum value at the weld centerline was much lower in the LZ. The LZ was therefore the softest zone. A stronger contribution of segregation is the possible explanation**.** In fact the hardness reduction respect to CZ hardness was not uniform along the hardness profiles but it was concentrated along the welding centerline.

The tensile strength and ductility for the joints and BM are shown in table 5. The BM was slightly stronger but much more ductile than FZ. The joints showed a loss of ductility that was higher than that of the strength. The samples processed at P_L equal to 3 KW, which had higher Mg contents and slightly lower porosity, were characterized by higher strength respect to those processed at higher P_L.

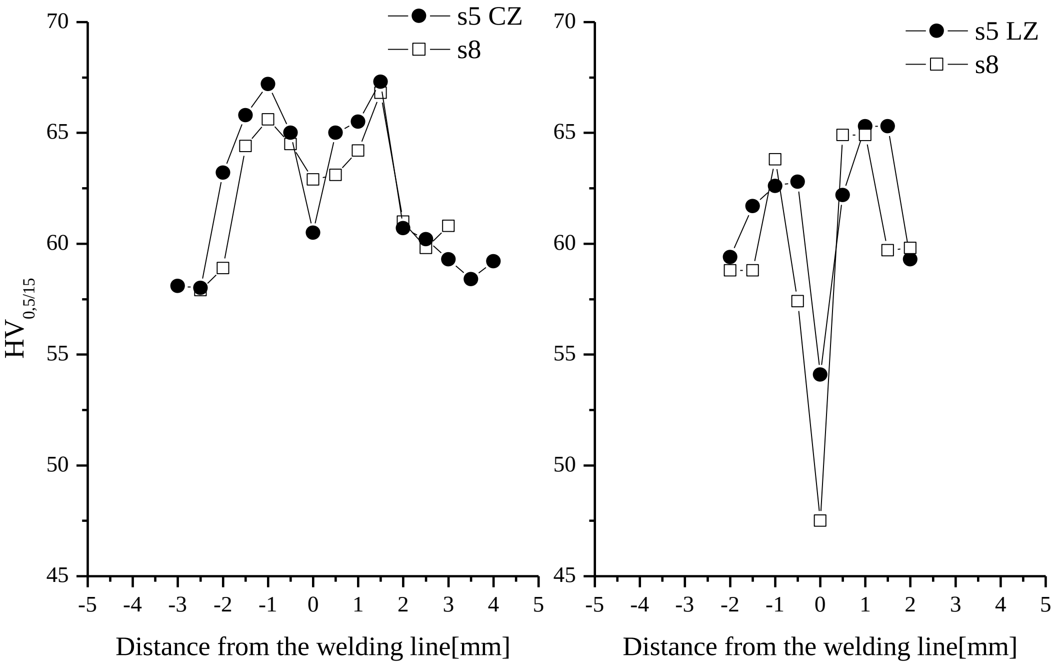

Fig. 11. Results of transverse microhardness for 5 and 8 weld, laser zone (right) and crown zone (left).

The joints fractured in the fused zone without necking evidence. The high loss of ductility with respect to BM was probably due to contribute of porosity and coarse segregated irregular second phase (Fig. 4) observed in the fusion zone [48].

Table 5 Tensile test results. All joints fractured in the LZ.

sample	TS [MPa]	E [%]	TS (efficiency %)	E (efficiency %)
4	206.9	10.8	84.7	64.9
5	201.4	11.1	82.4	66.7
6	194.9	7.1	79.7	42.6
7	178.4	6.1	73	36.6
8	193.8	9.4	79.3	56.2
9	186.6	7.5	76.4	44.7
BM	244.3	16.7	100	100

Fig. 12 presented the relationship between tensile properties and power ratio of hybrid joints. Tensile strength and ductility exhibited the same trend (Fig. 10). All the specimens fractured in the narrow FZ, which was the weakest zone according to the micro-hardness.

As discussed above, with respect to BM, the joints presented high grain size and Mg content. Mg content stiffened the molten zone by interacting with dislocations while coarser grain size softened the fused zone. Moreover, the porosity level reduced the strength of joint respect to that of BM due to a stress concentration on pores and reduction of useful area. From the analysis of the hardness, it can be thought that the Mg content can compensate or even overcome the softening due to the larger grain size. Therefore, the samples, characterized by higher Mg content and lower porosity level, were expected to have higher strength, which happened for 4, 5 and 6 samples (Fig. 8, 10).

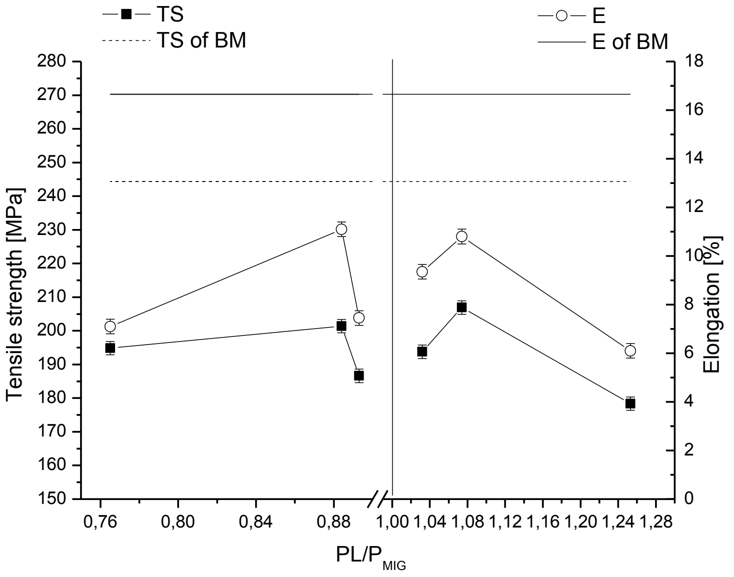

Fig. 12. Relationship between tensile strength (TS), elongation (E) and power ratio.

Both porosity and coarse segregated phases led to stress concentration so the cracks easy started from there and propagated throughout the section. Moreover, the coarse grain size of fused zones favored the crack tip mobility. A larger grain size resulted in a significant reduction of ductility for very similar porosity level (4-6). Therefore, coarse grain size, porosity and segregation observed in the fusion zone enhanced both crack initiation and mobility of crack tip. The ductility resulted sensitively lower respect to that exhibited by the base metal.

5. Conclusions

The quality assessment of the effect of power distribution in the arc assisted fiber laser welding of an Al-Mg alloy produced the following results.

1) The microstructure of the cross section bead presented fine equiaxed grains at the interface with BM. Columnar grains grew from the interface toward the weld centerline. Coarse equiaxed grains were found between the columnar grains. Segregation occurred mainly nearby the bead axis.
2) When laser power dominated the process (R>1), the average grain size variation was lower than that one of to the joints with dominant MIG power. The average Mg contents in the solid solution was higher than that of the BM. Higher P_L favorited the Mg evaporation.
3) Higher P_{MIG} and a lower R increased the CZ width. The underfill increased with P_{MIG} at the lowest P_L, which was due to the arc instability, and decreased for low P_{MIG} and high P_L.
4) When R ratio was closest to one, the smaller average grain size and geometrical defects were obtained along with high porosity level and low magnesium content. Porosity increased with the P_L.
5) In the HAZ, the hardness rose gradually from BM to the fine grain zone. The laser zone of the joint was the softest one. Segregation, porosity level, Mg content and coarse grain size affected negatively the strength and ductility of the weld.
6) The better power distribution for the mechanical properties was given by an average P_L and average/low P_{MIG}.

Acknowledgements

The authors thank a lot Mr. C. Todisco, Innovation Eng. Dept. University of Salento, for helping in the preparation of the metallographic samples.

References

[1] Ivan Bunaziv. Optimization of parameters for fiber laser-MAG hybrid welding in shipbuilding applications. (2013) Master's Thesis, Appeenranta University of Technology, Finland.

[2] J.M. Sanchez-Amaya, T. Delgado, L. Gonzàlez-Rovira, F.J. Botana. Laser welding of aluminum alloy 5083 and 6082 under conduction regime. Applied Surface Science 2009;225:9512-9521.

[3] J.M. Sanchez-Amaya, T. Delgado, J.J. De Damborenea, V. Lopez, F.J. Botana. Laser welding of AA 5083 samples by high power diode laser. Science and Technology of Welding and Joining 2009;14(1):78–86.

[4] T.Y. Kuo, H.C. Lin. Effects of pulse level of Nd-YAG laser on tensile properties and formability of laser weldments in automotive aluminum alloys. Materials Science and Engineering 2006;A 416:281–289.

[5] J. Yan, X. Zeng, M. Gao, J. Lai, T. Lin. Effect of welding wires on microstructure and mechanical properties of 2A12 aluminum alloy in CO_2 laser-MIG hybrid welding. Applied Surface Science 2009;255(16):7307–7313.

[6] L. D., Scintilla. Continuous-wave fiber laser cutting of aluminum thin sheets: Effect of process parameters and optimization. Optical Engineering 2014; 53(6), Article number 066113.

[7] L.P. Connor, Welding Handbook, eighth ed., American Welding Society, Miami, FL, 1987.

[8] N. Pierron, P. Sallamand, S. Mattei¨. Study of magnesium and aluminium alloys absorption coefficient during Nd:YAG laser interaction. Applied Surface Science 2007;253(6):3208–3214.

[9] M. Pastor, Zhao H., Martukanitz R.P., DebRoy T. Porosity, underfill and magnesium loss during continuous wave Nd:YAG laser welding of thin plates of aluminum alloys 5182 and 5754. American Welding Society, Miami, FL, USA, 1999;78:207-216.

[10] Almeida, A. Vilar, R. Alloy formation in laser surface alloying of Al with transition metals. Lasers in Engineering, 2008 (18 1-2), 2008:49-60

[11] J.E. Hatch. Aluminum: Properties and Physical Metallurgy, American Society for Metals, Metals, OH, 1984.

[12] M.J. Cieslak, P.W. Fuerschbach. On the weldability, composition, and hardness of pulsed and continuous Nd: YAG laser welds in aluminum alloys 6061, 5456, and 5086. Metall. Trans. 1988;19B:319–329.

[13] A. Ascari, A. Fortunato, L. Orazi, G. Campana, The influence of process parameters on porosity formation in hybrid LASER-GMA welding of AA6082 aluminum alloy. Optics & Laser Technology 2012;44:1485–1490.

[14] E. Le Guen, R. Fabbro, M. Carin, F. Coste, P. Le Masson Analysis of hybrid Nd:Yag laser-MAG arc welding processes. Optics & Laser Technology 2011;43:1155–1166

[15] M. El Rayes, C. Walz and G. Sepold. The influence of varius Hybrid welding parameters on bead geometry. Weld. J., 2004;83:147s–153s.

[16] Olsen, F., Hybrid laser-arc welding. Woodhead Publishing, Cambridge, UK, 2009.

[17] Y. B. Chen; Z. L. Lei; L. Q. Li; L. Wu. Experimental study on welding characteristics of CO_2 laser TIG hybrid welding process. Science and Technology of Welding & Joining 2006;11(4):403-411.

[18] M. Gao; X. Y. Zeng; Q. W. Hu; J. Yan. Weld microstructure and shape of laser–arc hybrid welding. Science and Technology of Welding and Joining, 2008;13(2):106-113.

[19] Liming Liu, Minghua Chen, Chenbin Li. Effect of electric arc on laser keyhole behavior based on direct observation during low power pulsed laser–arc hybrid welding process. Optics and Lasers in Engineering 2013;51:1153–1160.

[20] Ren D., Liu L., Li Y. Investigation on overlap joining of AZ61 magnesium alloy: laser welding, adhesive bonding, and laser weld bonding. Int J Adv Manuf Tech 2012;61:1–10.

[21] Jun Yan, Xiaoyan Zeng, Ming Gao, Jian Lai, Tianxiao Lin. Effect of welding wires on microstructure and mechanical properties of 2A12 aluminum alloy in CO_2 laser-MIG hybrid welding. Appl Surf Sci 2009;255:7307-7313.

[22] Katayama S., Naito Y., Uchiumi S., Mizutani M. Physical Phenomena and Porosity Prevention Mechanism in Laser-Arc Hybrid Welding. Transactions of JWRI, 2006;35(1), pp. 13-18.

[23] Quintino L, Costa A, Miranda R, Yapp D, Kumar V, Kong CJ. Welding with high power fiber lasers – a preliminary study. Materials & Design 2007;28:1231-7.

[24] G. Casalino, S.L. Campanellia, U. Dal Maso, A.D. Ludovico. Arc leading versus laser leading in the hybrid welding of aluminium alloy using a fiber laser. 8th CIRP Conference on Intelligent Computation in Manufacturing Engineering, Procedia CIRP 2013;12:151-156

[25] M. MazarAtabaki a, M.Nikodinovski b, P.Chenier c, J.Maa, W.Liu a, R.Kovacevic. Experimental and numerical investigations of hybrid laser arc welding of aluminum alloys in the thick T-joint configuration. Optics &LaserTechnology, 2014;59:68-92.

[26] Shaohua Yan, Yuan Nie, Zongtao Zhu, Hui Chen, Guoqing Gou, Jinpeng Yu, Guiguo Wang. Characteristic of microstructure and fatigue resistence of hybrid fiber laser-MIG welded Al-Mg alloy joint. Applied Surface Science 2014;298:12-18

[27] Dae-Won Cho, Won-Ik Cho, Suck-Joo Na. Modeling and simulation of arc: Laser and hybrid welding process. Journal of Manufacturing Processes 2014;16:26-55.

[28] J. R. Davis, ASM Handbook. Aluminum and aluminum alloy. Asm Specialty Handbook, 1993.

[29] I.J. Polmear, Light Alloy, Metallurgy of the Light Metals, Butterworth-Heinemann, Oxford, UK, 2000.

[30] Gao M., Cao T., Zeng X.Y., Lin T.X. Mechanical properties and microstructures of hybrid laser MIG welded dissimilar Mg-Al-Zn alloy. Sci Techonol Weld Join 2010;15:638-645

[31] David A. Porter and K. E. Easterling. Phase Transformations in Metals and Alloys. Chapman & Hall, London, UK, 1992.

[32] Mahrle A, Beyer E. Hybrid laser beam welding–classification, characteristics, and applications. Jornal of Laser Application 2006;18:169-80

[33] A. Verma, S. Kumar, P.S. Grant and K.A.Q. O'Reilly, Effect of cooling rate on the intermetallic phase formation in an AA6063 Al alloy, Journal of Alloys and Compounds 2013;555:274–282.

[34] Anhua Liu, Xinhua Tang, Fenggui Lu. Study on welding process and prosperities of AA5754 Al-alloy welded by double pulsed gas metal arc welding. Materials and Design 2013;50:149–155.

[35] L. F. Mondolfo, Aluminium alloys: structure and properties, 1976, London, Butterworth.

[36] Y. L. Liu and S. B. Kang. Solidification and segregation of Al-Mg alloys and influence of alloy composition and cooling rate. Mater. Sci. Technol., 1997;13:331–336.

[37] S. Das, N. S. Lim, H. W. Kim and C. G. Park. Effects of heat treatment on microstructure and mechanical properties of twin roll casted Al–5.5Mg–0.02Ti alloy. Materials & Design, 2010;31:3111–3115.

[38] Robert W. Messler, JR, Principles of Welding, John Wiley & Sons, Inc, 1999.

[39] JI J, Jasnau U, Seyffarth P. Gefügeverbesserung im Schweiβgut beim Nd:YAG-Laserstrahl-MSG-Hybridschweiβen von Aluminiumlegierungen. Schweiβen und Schneiden 2007;59(11):608-612.

[40] Liming Liu, Xinfeng Hao. Improvement of laser keyhole formation with the assistance of arc plasma in the hybrid welding process of magnesium alloy. Optics and Lasers in Engineering 2009;47:1177–1182

[41] Ming Gao, Hai-Guo Tang, Xiao-Feng Chen, Xiao-Yan Zeng. High power fiber laser arc hybrid welding of AZ31B magnesium alloy. Materials and Design 2012;42:46–54.

[42]Y. B. Chen, Y. B. Zhao, Z. L. Lei and L. Q. Li. Effects of laser induced metal vapour on arc plasma during laser arc double sided welding of 5A06 aluminium alloy. Science and Technology of Welding and Joining 2012;17(1).

[43] Liming Liu, Minghua Chen, Chenbin Li. Effect of electric arc on laser keyhole behavior based on direct observation during low power pulsed laser–arc hybrid welding process. Optic and Lasers Engineering 2013;51:1153-1160.

[44] A.W.AlShaer, L.Li, A. Mistry. The effects of short pulse laser surface cleaning on porosity formation and reduction in laser welding of aluminium alloy for automotive. Optics &LaserTechnology 2014;64:162–171

[45] M. Mazar Atabaki, M. Nikodinovski, P. Chenier, J. Maa, W. Liu, R. Kovacevic. Experimental and numerical investigations of hybrid laser arc welding of aluminum alloys in the thick T-joint configuration. Optics & Laser Technology 2014;59:68–92.

[46] Christian B. Fuller, Albert R. Krause, David C. Dunand, David N. Seidman. Microstructure and mechanical properties of a 5754 aluminum alloy modified by Sc and Zr additions. Materials Science and Engineering 2002;A338:8-16.

[47] S. Lathabai, P.G. Lloyd. The effect of scandium on the microstructure, mechanical properties and weldability of a cast Al–Mg alloy. Acta Materialia 2002;50:4275–4292.

[48] G.E Dieter, Mechanical Metallurgy, McGraw-Hill, London, UK, 1988.